The impact of atmospheric motion on source-specific black carbon and the induced direct radiative effect over a river-valley region

Huikun Liu[1], Qiyuan Wang[1,2,4*], Suixin Liu[1,5], Bianhong Zhou[3], Yao Qu[1], Jie Tian[1], Ting Zhang[1], Yongming Han[1,2,4], Junji Cao[6,5*]

[1]State Key Laboratory of Loess and Quaternary Geology, Institute of Earth Environment, Chinese Academy of Sciences, Xi'an, 710061, China
[2] CAS Center for Excellence in Quaternary Science and Global Change, Xi'an, 710061, China
[3] Shaanxi Key Laboratory of Disaster Monitoring and Mechanism Simulation, College of Geography & Environment, Baoji University of Arts & Sciences, Baoji 721013, China
[4]Guanzhong Plain Ecological Environment Change and Comprehensive Treatment National Observation and Research Station, Xi'an 710061, China
[5]Shaanxi Key Laboratory of Atmospheric and Haze-fog Pollution Prevention, Xi'an 710061, China
[6]Institute of Atmospheric Physics, Chinese Academy of Sciences, Beijing 100029, China

*Correspondence to: Qiyuan Wang (wangqy@ieecas.cn) and Junji Cao (jjcao@mail.iap.ac.cn)

Abstract. Black carbon (BC) has a strong light absorption ability and is known as the second strongest light-absorbing substance in the atmosphere after CO_2. Atmospheric motion plays an important role in the ambient mass concentrations of pollutants. The relationship between atmospheric motion and BC aerosols is complex, and detailed investigation of the impact of different scales of motion on BC is still insufficient. Thus, an intensive observation was launched in a typical river-valley city. Equivalent BC (eBC) source apportionment was conducted using the aethalometer model with the site-dependent absorption Ångström exponents (AAEs) and the mass absorption cross-sections (MACs) which were retrieved using a positive matrix factorization (PMF) model based on observed chemical data and optical data. The derived AAEs were 1.07 for diesel vehicular emissions, 2.13 for biomass burning, 1.74 for coal combustion, and 1.78 for mineral dust. The mean values of eBC_{fossil} and $eBC_{biomass}$ were 2.46 µg m^{-3} and 1.17 µg m^{-3} respectively. A self-organizing map showed that four featured atmospheric motions categories were identified at the sampling site. A further analysis of eBC under the four motion categories showed that the BC pollution was more likely to happen when the influence of local-scale motion outweighed that of regional-scale motion. The trajectory clusters indicate that air mass direction could post divergent impacts under different scales of atmospheric motion. The direct radiative effects (DRE) of source-specific eBCs were lower when the influence of regional-scale motion outweighed that of the local one. However, the DRE efficiencies under the dominance of regional scale motion were ~1.5 times higher than those under the dominance of local scale motion. This study revealed the disproportional change between BC mass concentration and its DRE. The DRE efficiency of BC was enhanced during the regional transport which could lead to greater consequences in receptor regions. It highlights the regionally transported BC and its potentially enhanced climatic effect are worthy of attention.

1

1 Introduction

Black carbon (BC) is commonly produced by the incomplete combustion of biomass and fossil fuels. It has a strong light absorption ability to heat the atmosphere, which has been widely recognized as the second strongest light-absorbing substance in the atmosphere after CO_2 (Bond et al., 2013). Due to its high light-absorbing ability, BC has considerable potential to cause radiative perturbation in the radiative balance between earth and atmosphere. The balance is so important that breaking it will result in climate change, leading to further negative changes in the ecosystem (Schroter et all., 2005). Those changes ultimately will threaten humans' food security and biodiversity (Ochoa-Hueso et al., 2017; Shindell et al., 2012). Besides heating the atmosphere directly, BC is also an important cloud nucleus leading to indirect climatic effects after being activated (Jacobson, 2002). Thus, BC is also known as a short-lived climate pollutant, but its climatic effect is highly variable depending on its radiative efficiency and lifetime (IPCC, 2021).

The radiative efficiency of BC may be variable because of different emission sources and atmospheric aging processes (Bond et al., 2013; He et al., 2015; Cappa et al., 2012). Source-specific BCs possess divergent light absorbing abilities (Cheng et al., 2011) which leads to different radiative effects. In addition to different emission sources, regional transport could also impact the light-absorbing ability via the aging process (Zhang et al., 2019). After being emitted, BC can stay in the atmosphere for days (IPCC, 2021). During transport, fresh BC will experience a series of physical and chemical changes for instance, mixing with other substances and altering its microphysical characteristics, resulting in changes in optical properties (Kahnert and Kanngießer, 2020). This process may be even faster in polluted regions (Peng et al., 2016), as a result enhancing the light-absorbing ability of BC. The experiment showed that the absorption ability of BC after aging could be as high as 2.4 times that in its fresh state (Peng et al., 2016).

A local concentration of BC is controlled by the local emission sources and meteorological conditions as well as regional transport. Normally, local emission sources are predictable at to some degree in urban areas because emission sources are mainly anthropogenic and the concentration of pollutants follow the diurnal cyclic patterns of anthropogenic activities in a relatively short period. By contrast, meteorological conditions and regional transport are governed by multiply scales of motion which results in a distinct meteorological impact on ambient pollutant concentrations (Levy et al., 2010, Dutton, 1976). A commonly accepted classification of the scale of motion involved horizontal distance and time scales. Typically, the time scale of local-scale motion varies from hours to days and the space scale (it is atmosphere phenomena) ranges from 10^2 to 10^5 m (Oke et al., 2002; Seinfeld and Pandis, 2006). The local scale of motion is mainly controlled by local factors such as the roughness of the earth's surface and aerosol concentration (Hewitson and Crane, 2006; IPCC, 2021). A larger scale of motion is associated with a mesoscale or synoptic scale weather system, which on the one hand can carry pollutants and on the other, diffuse them (Kalthoff et al., 2000; Zhang et al., 2012).

The relationship between atmospheric motion and pollution is complex. Atmospheric motion decides where and how extensive the pollution could be, but pollutant concentration itself is a local factor (Dutton, 1976). Liao et al., (2020) found that synoptic-scale flow led to an enhanced level of $PM_{2.5}$ in a coastal area of the Pearl River Delta, while meso/local scale motion led to $PM_{2.5}$ pollution in the inland area. Levy et al. (2010) showed that the concentrations of NO_x and SO_2 were higher under the dominance of smaller-scale motion than under larger scale motion. However, few studies have touched on the impacts of

70 different scales of motion on BC and its radiative efficiency even though it could lead to rapid climatic effects due to its uneven

71 and constantly changing distribution (IPCC, 2021).

72 Topography also plays an important role in air pollution (Zhao et al., 2015). The topography of the river-valley city is

73 complicated which has a considerable influence on air pollution and synoptic patterns (Green et al., 2016; Carvalho et al., 2006).

74 The pollution level of the river-valley city is influenced by general atmospheric dynamics and strongly impacted by the local

75 scale of dynamics (Brulfert et al., 2006). With the uneven solar radiation due to different albedo and surface roughness, it is

76 easy to form a different local scale of circulation but it can plays an important role in changes in pollutant mass concentration

77 (Wei et al., 2020). Once pollutants are produced or transported in, it is hard to disperse them due to the blocking effect of the

78 mountains and then the pollutants could be carried by the airflows over the river-valley terrain converge at the bottom of the

79 valley (Zhao et al., 2015).

80 Thus, we are fascinated to study the impact of different scales of motion on source-specific eBCs and their radiative effects

81 over a river-valley city. The primary objectives of this study were: (1) to quantify the eBC contributions from fossil fuel

82 combustion and biomass burning, (2) to investigate the impacts of different featured scales of motion on the source-specific

83 eBC, and (3) to estimate the radiative effects and the radiative efficiency of the source-specific eBC under different atmospheric

84 motions. Thus the study provides insights into the influence of the specified atmospheric motions on BC and highlights the

85 radiative efficiency and potential climatic effect of the regionally transported BC.

2 Methodology

2.1 Research site

88 Guanzhong Plain is surrounded by mountains to the north and south, and is high in the west but low in the east forming a

89 trumpet shape toward the east. This terrain causes divergent local scales of air movement which produce different impacts on

90 pollution (Wei et al., 2020). Mountains significantly affect pollution, since they block the wind in the vicinity of the mountains

91 but accelerate it along the river (Zhao et al., 2015). The valley not only performs as a drain for pollutants but also acts as a way

92 for pollutants to enter the area, therefore aggravating pollution. Baoji is a typical river-valley city (Figure S1), locates at furthest

93 west of the Guanzhong Plain and suffers severe pollution in winter. Baoji is also an important railway intersection in China

94 connecting six railways to the north-west and southwest China. Due to its special topographic conditions, dense population,

95 and major highway and railway networks, it is not easy to disperse pollutants. The sampling site is on the top of the Arts and

96 Sciences building at Baoji University (34°21′ 18.4″ N, 107°8′ 34.7″ E) surrounded by commercial and residential buildings,

97 highways, and rivers.

2.2 Sampling and laboratory measurements

99 Equivalent BC (eBC) and the absorption coefficient (b_{abs}) at 370, 470, 520, 590, 660, 880, and 950 nm wavelength were

100 measured using an AE33 aethalometer (Magee Scientific, Berkeley, CA, USA) via a $PM_{2.5}$ cut-off inlet (SCC 1.829, BGI Inc.

101 USA) with a time resolution of 5 min. A Nafion® dryer (MD-700-24S-3; Perma Pure, Inc., Lakewood, NJ, USA) with a flow

102 rate of 5 L min^{-1} was used to dry the $PM_{2.5}$ before the measurement. Briefly, particles were dried by the Nafion dryer before

103   being measured with the AE33 aethalometer, and the deposited particles were irradiated with seven wavelengths of light-

104   emitting diodes (λ = 370, 470, 520, 590,660, 880, and 950 nm) and the light attenuation was detected. The non-linear loading

105   issue for filter-based absorption measurement is solved by a technique in AE33 called dual-spot compensation. The quartz filter

106   matrix scattering effect was corrected by using a factor of 2.14. More details of AE33 measurement techniques can be found

107   in Drinovec et al. (2015). The scattering coefficient (b_{scat}) at 525 nm wavelength was measured by a nephelometer (Auora-

108   1000, Ecotech, USA) with a time resolution of 5 min during the study period. It operated simultaneously with AE33 using the

109   same $PM_{2.5}$ cyclone and Nafion dryer. A single wavelength (525nm) was used to measure the scattering coefficient. The

110   calibration was conducted based on the user guide with calibration gas R-134. The zero calibration was conducted every other

111   day by using clean air without particles. The ambient air was sucked in through a heated inlet with a flow rate of 5 L min^{-1}. The

112   relative humidity remained lower than 60%.

113    $PM_{2.5}$ samples were collected for every 24 hours (h) from 10 a.m. local time to the 10 a.m. the next day from 16th November

114   2018 to 21st December 2018 by two sets of mini-volume samplers (Airmetrics, Oregon, USA) using quartz fiber filters (QM/A;

115   Whatman, Middlesex, UK) simultaneously with Teflon filters (Pall Corporation, USA) with a flow rate of 5 L min^{-1}. Those

116   samples were kept in a refrigerator at 4°C before analysis. The mass concentration of K^+ in the $PM_{2.5}$ sample was extracted and

117   determined by a Metrohm 940 Professional IC Vario (Metrohm AG., Herisau, Switzerland) with an IonPac CS12A column

118   (20m methane sulfonic acid as the eluent) for cation analysis. Elements (i.e. Mg, Al, Si, S, Cl, Ca, V, Mn, Fe, Ni, Cu, As, Se,

119   Br, Sr, Pb, Ga, and Zn) were determined by energy-dispersive x-ray fluorescence (ED-XRF) spectrometry (Epsilon 4 ED-XRF,

120   PANalytical B.V., Netherlands). The X-ray is from a gadolinium anode on a side-window X-ray tube. A spectrum of the ratio

121   of X-ray and photon energy was obtained after 24 minutes of analysis for each sample. Each energy peak represents a specific

122   element. The peak area indicates the concentration of the element. Quality control is conducted on a daily basis with testing

123   sample PAT-3195. Organic carbon (OC) and elemental carbon (EC) in each sample were determined by a DRI Model 2001

124   Thermal/Optical Carbon Analyzer (Atmoslytic Inc., Calabasas, CA, USA). The thermal/optical reflectance (TOR) method and

125   IMPROVE_A protocol were used for analysis. A punch of a quartz filter sample was heated at different temperatures to obtain

126   data for four OC fractions and three EC fractions. Total OC was calculated by summing all OC fractions and the produced

127   pyrolyzed carbon. Total EC was calculated by summing all EC fractions minus pyrolyzed carbon (OP). Detailed methods and

128   quality assurance/quality control processes were described in Cao et al., (2003). Primary organic carbon (POC) was estimated

129   by using the minimum R-squared (MRS) method which is based on BC as a tracer method. It uses the minimum R^2 between

130   OC and BC to indicate where the ratio of secondary OC and BC is independent. A detailed description of the MRS method can

131   be referred to in Wu et al., (2016). The NO_x, wind speed, and direction at 12 ground monitoring sites were downloaded from

132   http://sthjt.shaanxi.gov.cn/hx_html/zdjkqy/index.html. The wind data at 100 meters (m) above the ground and the planetary

133   boundary layer height were downloaded from https://rda.ucar.edu/datasets/ds633.0. The data used for trajectory analysis was

134   downloaded from Global Data Assimilation System (GDAS, https://www.ready.noaa.gov/gdas1.php).

135   **2.3 Optical source apportionment**

136   The positive matrix factorization (PMF) model was used for the optical source apportionment in this study. PMF solves

137   chemical mass balance by decomposing the observation data into different source profiles and contribution matrices as follows:

138 $\quad X_{ij} = \sum_{k=1}^{p} g_{ik} f_{kj} + e_{ij}$ (1)

139 where X_{ij} denotes the input data matrix; p is the number of sources selected in the model; g_{ik} denotes the contribution of the

140 k^{th} factor to the ith input data; f_{kj} represents the kth factor's profile of the jth species; and e_{ij} represents the residual. Both g_{ik} and

141 f_{kj} are non-negative. The uncertainties of each species and $b_{abs}(\lambda)$ were calculated by the equation recommended in EPA

142 PMF5.0 (Norris et al, 2014) user guideline as follows:

143 $\quad Unc = \sqrt{(error\ fraction \times concentration)^2 + (0.5 \times MDL)^2}$ (2)

144 $\quad Unc = \frac{5}{6} \times MDL$ (3)

145 where MDL is the minimum detection limit of data. The error fraction of offline measured data is the difference between the

146 measured values of the same sample. An error fraction of 0.1 was used for online data (Rai et al., 2020). PMF solves the

147 equation by minimizing the Q value as follows, which is the sum of the normalized residuals' square:

148 $\quad Q = \sum_{i=1}^{n} \sum_{j=0}^{n} \left[\frac{e_{ij}}{u_{ij}} \right]^2$ (4)

149 where u_{ij} represents the uncertainties of each X_{ij} and Q_{true}/Q_{exp} were used as the indicators for factor number determination.

150 **2.4 eBC source apportionment**

151 eBC generated from biomass burning and fossil fuel combustion were separated by an aethalometer model (Sandradewi et. al.,

152 2008). Different from the traditional aethalometer model, an improvement has been made by giving consideration to the

153 interference of the b_{abs} at a lower wavelength (370nm) caused by dust and secondary OC. Thus, the calculation of the absorption

154 and source apportionment was conducted by the following equations (Wang et al., 2020):

155 $\quad \frac{b_{abs}(370)_{fossil}}{b_{abs}(880)_{fossil}} = \left(\frac{370}{880}\right)^{-AAE_{fossil}}$ (5)

156 $\quad \frac{b_{abs}(370)_{biomass}}{b_{abs}(880)_{biomass}} = \left(\frac{370}{880}\right)^{-AAE_{biomass}}$ (6)

157 $\quad b_{abs}(880) = b_{abs}(880)_{fossil} + b_{abs}(880)_{biomass}$ (7)

158 $\quad b_{abs}(370) = b_{abs}(370)_{fossil} + b_{abs}(370)_{biomass} + b_{abs}(370)_{secondary} + b_{abs}(370)_{dust}$ (8)

159 $\quad eBC_{fossil} = \frac{b_{abs}(880)_{fossil}}{MAC_{BC}(880)_{fossil}}$ (9)

160 $\quad eBC_{biomass} = \frac{b_{abs}(880)_{biomass}}{MAC_{BC}(880)_{biomass}}$ (10)

161 where AAE_{fossil} and $AAE_{biomass}$ are the AAEs for fossil fuel combustion and biomass burning. They were derived from the

162 optical source apportionment by using PMF as discussed in section 3.1. $b_{abs}(370)$ and $b_{abs}(880)$ are the total b_{abs} measured by

163 AE33 at the wavelengths of 370 nm and 880 nm respectively. $b_{abs}(370)_{fossil}$ and $b_{abs}(880)_{fossil}$ were the b_{abs} caused by emissions

164 from fossil fuel combustion at those two wavelengths. $b_{abs}(370)_{biomass}$ and $b_{abs}(880)_{biomass}$ are the b_{abs} caused by emissions from

165 biomass burning at those two wavelengths. $b_{abs}(370)_{dust}$ refers to b_{abs} contributed by mineral dust at the wavelength of 370 nm,

166   which was derived from the result of optical source apportionment. $b_{abs}(370)_{secondary}$ refers to the b_{abs} caused by the secondary

167   aerosols at the wavelength of 370 nm, which was calculated by the minimum R-squared approach with eBC as a tracer (Wang

168   et al., 2019). eBC$_{fossil}$ and eBC$_{biomass}$ were the eBC of fossil fuel combustion and biomass burning. $MAC_{BC}(880)_{fossil}$ and

169    $MAC_{BC}(880)_{biomass}$ are the mass absorption cross-section of eBC$_{fossil}$ and the mass absorption cross-section of eBC$_{biomass}$ at the

170   wavelength of 880 nm respectively, which were calculated based on the result of the optical source apportionment using PMF.

171   **2.5 Indicators for the different scale of motion**

172   The mathematical definitions of airflow condition proposed by Allwine and Whiteman (1994) were used in this study. The

173   definitions quantify the flow features integrally at individual stations. Three variables were quantified, namely actual wind run

174   distance (S) which is the scalar displacement of the wind in 24 h, the resultant transport distance (L) which is the vector

175   displacement of the wind in 24 h, and the ratio (R) of L and S which indicates the difference between the wind run distance and

176   the actual resultant distance, representing the frequency of the wind veering in 24 h. To distinguish the influence of different

177   scales of atmospheric motions, based on the method proposed by Levy et al., (2010), we used wind data at 100 m above the

178   sampling site and the wind data from 12 monitoring stations at ground level (~15m) to indicate the different featured scales of

179   motions. The winds at surface monitoring stations were expected to be more sensitive to local-scale turbulence and convection

180   than winds at 100 m height. With less influence of surface forces, the indicators at 100 m would be more sensitive to larger

181   scales of motion. Equations are as follows:

182    $$L_{n\tau/bj} = T\left[\left(\sum_{j=i}^{i-\tau+1} u_i\right)^2 + \left(\sum_{j=i}^{i-\tau+1} v_i\right)^2\right]^{1/2} \tag{11}$$

183    $$S_{n\tau/bj} = \sum_{j=i}^{i-\tau+1}(u_j{}^2 + v_j{}^2)^{1/2} \tag{12}$$

184    $$R_{n\tau/bj} = 1 - \frac{L_{i\tau}}{S_{i\tau}} \tag{13}$$

185   where T is the interval of the data (i.e., 60 min), i is the ith number of data, τ is the integration time period of the wind run (24

186   h), and n is the number of monitoring stations (a total of 12 in this study). With the wind data from the 12 monitoring stations

187   covering Baoji, the L and S at the 12 different sites at ground level were calculated. $L_{n\tau}$ and $S_{n\tau}$ represented the resultant transport

188   distance and the actual wind run distance at the nth monitoring station at ground level; $R_{n\tau}$ is the recirculation factor at the nth

189   monitoring station which is the ratio calculated by $L_{n\tau}$ and $S_{n\tau}$. L_{bj}, and S_{bj} are the resultant transport distance and the actual

190   wind run distance at 100 m height to represent the flow characteristics higher in the atmosphere at the study site, which was

191   calculated by using wind data at 100 m height. R_{bj} is the ratio at 100 m height calculated using L_{bj} and S_{bj}.

192   As explained in Levy et al., (2010), if local-scale motion is strong and regional-scale motion is weak, then winds at each

193   monitoring site would be mainly controlled by local-scale motion. The variations of winds at each station would not be likely

194   to be uniform due to different local factors, resulting in a relatively large standard deviation (R_{std}) of the $R_{n\tau}$ calculated by using

195   the wind speed and direction data from the 12 monitoring stations in Baoji. Otherwise, the influence caused by small-scale

196   differences would be weakened, the wind direction would be likely to be more uniform over a large area, and the R_{bj} and the

197   R_{std} should be relatively smaller.

Atmospheric
Chemistry
and Physics
Discussions

198   **2.6 Self-organizing map**

199   A self-organizing map (SOM) is one type of artificial neural network developed by Kohonen (1990), which is widely used for

200   categorizing high-dimensional data into a few major features (Stauffer et al., 2016 and Pearce et al., 2014). It is widely used

201   for categorizing different meteorological patterns (Liao et al., 2020; Han et al., 2020; Jiang et al., 2017). Different from the

202   traditional dimension reduction method (e.g., principal component analysis), it projects high-dimensional input data into user-

203   designed lower-dimension which is typically a two-dimensional array of nodes by non-linear projection (Hewitson and Crane,

204   2006). Its performance in classifying climatological data showed robust result (Reusch et al., 2005). Therefore, SOM was

205   conducted to categorize the daily atmospheric motions in the study period to explore the influences of different scales of motion

206   on source-specific eBC. Three sets of data (R_{std}, L_{bj}, and S_{bj}) were input into SOM. Determining the size of the output map is

207   crucial for SOM. To reduce the subjective determination, the K-means cluster method was used for size decision-making. The

208   similarity of each item of input data and node was measured using Euclidean distance. The iteration number was set to 2000.

209   For each input data item, the node closest to it will "win out". The reference vectors of the winning node and their neighborhood

210   nodes will update and adjust towards the data. The "Kohonen" package in R language was used to develop the SOM model in

211   this study.

212   **2.7 Estimations of direct radiative effects and heating rate**

213   The Santa Barbara DISORT Atmospheric Radiative Transfer (SBDART) model was used to estimate the DRE induced by

214   source-specific eBC. The model has been used in many studies to calculate the DRE caused by aerosols and BC (Pathak et al.,

215   2010; Rajesh et al., 2018; Zhao et al., 2019). SBDART calculated DRE based on several well-tested physical models. The

216   model was elaborated in Ricchiazzi et al., (1998). The important input data includes aerosol parameters which contain aerosol

217   optical depth (AOD), single scattering albedo (SSA), asymmetric factor (AF) and extinction efficiency, surface albedo, and

218   atmospheric profile. Aerosol parameters used in this study were derived by the Optical Property of Aerosol and Cloud (OPAC)

219   model (Hess et al., 1998) based on the number concentrations of aerosol components. Since the study was conducted in the

220   urban region, the urban aerosol profile was used in OPAC, which includes soot (eBC), water-soluble matter (WS), and water-

221   insoluble matter (WIS). The number concentration of soot was derived from the mass concentrations of eBC with the default

222   ratio in the model. The number concentration of WS and WIS were adjusted until the modeled SSA and b_{abs} at 500nm in OPAC

223   were close ($\pm5\%$, see Figure S2) to those values calculated with data from the nephelometer and AE33 ($b_{ext}(520) = b_{scat}(525)$

224   + $b_{abs}(520)$, SSA= $b_{scat}(525)/b_{ext}(520)$). The DRE of source-specific eBC at the top of atmosphere (TOA) and surface

225   atmosphere (SUF) was calculated from the difference between DREs with or without the number concentration of the source-

226   specific eBC under clear-sky conditions.

227   $$DRE_{eBC} = (F\downarrow - F\uparrow)_{with\ eBC} - (F\downarrow - F\uparrow)_{without\ eBC} \tag{14}$$

228   $$DRE_{eBC,ATM} = DRE_{eBC,TOA} - DRE_{eBC,SUF} \tag{15}$$

229   where DRE_{eBC} is the DRE of source-specific eBC, $F\downarrow$ and $F\uparrow$ are the downward and upward flux, $DRE_{eBC,ATM}$ is the DRE of

230   the source-specific eBC at the whole atmosphere which is equal to the DRE at the top of the atmosphere ($DRE_{eBC,TOA}$) minuses

231   that at the surface ($DRE_{eBC,SUF}$).

232   **3 Results and discussion**

233   **3.1 Calculation of eBC$_{fossil}$ and eBC$_{biomass}$**

234   To obtain the site-specific AAEs and MACs for calculating the source-specific eBC with the improved aethalometer model,

235   the PMF model was used for the optical source apportionment. For every solution, PMF was runed 20 times. Q_{true}/Q_{exp} from 2-

236   factors solution to 7-factors solution was examined, and the values of a 4-factors solution was found most stable compared with

237   others because the Q_{true}/Q_{exp} values did not drop appreciably after adding one more factor (Figure S3). Thus, a 4-factors source

238   number was determined. The Bootstrap (BS) and Displacement (DISP) methods were also conducted for robustness and

239   stability (Table S1) with the result showing that there was no swap for the 4-factors solution. The modelled primary $b_{abs}(\lambda)$

240   were well correlated (r = 0.95~0.96, slope = 0.90~0.95, p < 0.01, Figure S4) with their observed counterparts, which suggested

241   that the modelling performance of PMF5.0 was good. The factor profiles given by PMF are shown in Figure 1.

242   The first factor was featured with high loadings of EC (52%), POC (49%), and V (49%) and moderate loadings of Mn (33%),

243   Ni (40%), Cu (37%), and Zn (44%). This factor source contributed 27% to 44% of primary $b_{abs}(\lambda)$. High amounts of EC were

244   found associated with vehicular emissions due to incomplete fuel combustion (Cao et al., 2013). V and Ni are commonly

245   detected in the particles emitted by diesel-powered vehicles (Lin et al., 2015 and Zhao et al., 2021). Mn compound is commonly

246   used as an antiknock additive for unleaded gasoline to raise octane value and protect the engine (Lewis et al., 2003; Geivanidis

247   et al., 2003). Cu and Zn were found in the combustion of lubrication oil and wearing parts (i.e., brakes and tires) (Thorpe and

248   Harrison, 2008; Song et al., 2006). In addition, the EC associated with this factor was found well correlated (r = 0.83, p < 0.01,

249   Figure S5) with the daily averaged NO$_x$ data which is a commonly used tracer of vehicular emissions in the urban area (Zotter

250   et al., 2017). According to recent research on the source contributions of BC emissions, the majority of BC from transportation

251   was emitted by on-road diesel vehicles in China (Xu et al., 2021). Owing to those results above, this factor was identified as

252   diesel vehicular emissions. The MAC of this factor (MAC (880)$_{diesel}$) was 6.7 m^2 g^{-1}. The estimated AAE of this factor (AAE$_{diesel}$)

253   was 1.07 which is comparable with the AAE values of vehicle emissions (0.8~1.1) reported in previous studies (Zotter et al.,

254   2017; Kirchstetter et al., 2004).

255   The second factor was characterized by the high loading of K$^+$ (51%), Cl (79%), and Br (52%) and moderate amounts of EC

256   (26%), POC (28%), and Pb (30%). K$^+$ is one of the widely recognized tracers for the emissions of biomass burning (Urban et

257   al., 2012; Zhang et al., 2015). High loading of Cl also can be taken as a signal of biomass burning (Yao et al., 2002; Manousakas

258   et al., 2017). Previous studies reported that a large amount of Br was found in biomass burning aerosols because of the CH$_3$Br

259   emission during combustion (Manö and Andreae, 1994; Artaxo et al.,1998). OC and EC are commonly found in particulate

260   matter emitted from biomass burning as major substances (Song et al, 2006). Pb was also observed in biomass-burning aerosols

261   (Amato et al., 2016). Owning to the existence of brown carbon in the biomass-burning aerosols (Wang et al., 2019), the

262   contribution of this factor to primary $b_{abs}(370)$ was as high as 50%, but only 33% to primary $b_{abs}(880)$. Thus, this factor was

263   identified as biomass burning. The MAC of this factor (MAC (880)$_{biomass}$) was 9.5 m^2 g^{-1}. The AAE of this factor (AAE$_{biomass}$)

264   was 2.13 which fell in the wide range of biomass-burning AAE (1.2~3.5) (Sandradewi et al., 2008; Helin et al., 2018; Zotter et

265   al., 2017).

266   The third factor presented significant loadings of S (64%), Se (98%), As (51%), and Pb (53%) and moderate loadings of Ga

267   (42%), which were found highly associated with coal combustion (Hsu et al., 2016; Tan et al., 2017). As China began to phase

268   out Pb-containing gasoline, coal combustion gradually became a main source of Pb in $PM_{2.5}$ (Xu et al. 2012). Thus, this factor

269   was assigned to coal combustion. The MAC of this factor (MAC $(880)_{coal}$) was 7.5 m^2 g^{-1}. This factor contributed 17%~19%

270   primary $b_{abs}(\lambda)$, and its derived AAE_{coal} was 1.74 which is close to the AAE of coal-chunks (Sun et al., 2017).

271   The last factor is dominated by the contributions of Al (68%), Si (76%), Ca (65%), Fe (51%), and Sr (71%). Those elements

272   were typical crustal elements which are found abundantly in mineral dust (Tao et al., 2016; Tao et al., 2017). The minor amounts

273   of EC in crustal dust could be from other EC sources deposited on the ground and later the mixed particles were resuspended

274   by natural or artificial disturbance (e.g., wind and traffic flow), with the result that a tiny portion of EC was found in the dust.

275   This factor only contributed ~4% of primary $b_{abs}(\lambda)$. The estimated AAE_{dust} was 1.78 which is close to the AAE of mineral dust

276   reported in previous studies ($AAE_{370\sim950}$=1.82, Yang et al., 2009).

277   As elaborated above, EC in $PM_{2.5}$ over Baoji was mainly from diesel vehicular emissions, biomass burning, and coal

278   combustion, which can be categorized into biomass burning and fossil fuel combustion (the sum of diesel vehicular emissions

279   and coal combustion). Thus, the AAE_{fossil} (1.26) and MAC $(880)_{fossil}$ (7.1 m^2 g^{-1}) was calculated by averaging the AAE_{coal} (MAC

280   $(880)_{coal}$) and AAE_{diesel} (MAC $(880)_{diesel}$) given their mass contributions to EC (Table S2). The hourly mass concentrations of

281   eBC_{fossil} and $eBC_{biomass}$ were then calculated using the 'aethalometer model' (Eqs. 5–10). The results showed that eBC_{fossil} and

282   $eBC_{biomass}$ barely shared a correlation (r = 0.3, p < 0.01, Figure S6), indicating a reasonably good separation. Their diurnal

283   variations showed varied, however (Figure 2). The mean values of eBC_{fossil} and $eBC_{biomass}$ were 2.46 μg m^{-3} and 1.17 μg m^{-3},

284   respectively. The diurnal variation of eBC_{fossil} (Figure 2a) showed a bimodal pattern with two peaks at 9 a.m. and 7 p.m. which

285   were typical commuting peak hours in cities, indicating a strong influence of traffic emissions. Due to the reduced traffic flow

286   from 1 a.m. to 5 a.m., eBC_{fossil} decreased slowly. After 5 a.m. passenger vehicles were allowed on the highway and eBC_{fossil}

287   started to rise, perhaps owing to pollutant transport from nearby highways. As the morning commute peak led to increased

288   vehicles on the road in the city, eBC_{fossil} reach its first peak at 9 a.m. From 9 a.m. to 11 a.m., eBC_{fossil} only declined slightly

289   because reduced wind speed (Figure 2c) offset the effect of the decline in traffic flow. From 11 a.m. to 3 p.m., the increased

290   planetary boundary layer height (PBLH) (Figure 2d) led to a rapid decrease of eBC_{fossil}. Later PBLH shrank fast, resulting in

291   eBC_{fossil} rising and the evening traffic peak, coupled with the undesirable dispersion conditions, helped eBC_{fossil} skyrocket to

292   its second peak at 7 p.m. After passing the evening traffic peak hours, the reduced traffic flow led to eBC_{fossil} declining

293   dramatically again. New para here

294   By contrast, the diurnal variation of $eBC_{biomass}$ (Figure 2b) showed more influence from meteorological conditions during the

295   daytime, demonstrating a lower concentration during the day and higher concentration at night. After 6 p.m., increased biomass

296   burning emitted more $eBC_{biomass}$ and the stable PBLH hindered the dispersion of $eBC_{biomass}$, which together pushed $eBC_{biomass}$

297   to reach its peak at 8 p.m. Afterward, the downslope wind from the mountain converged in the valley at night time (Oke et al.,

298   2002) and moved easterly where the altitude is lower than Baoji (Zhao et al., 2015), which led to the raised wind speeds (Figure

299   2c) and reduced $eBC_{biomass}$ pollutant levels.

3.2 The influence of regional and local atmospheric motion on eBC$_{fossil}$ and eBC$_{biomass}$

The K-means result showed that the four-categories solution was more appropriate (Figure S7). Thus a 2×2 map size was used in SOM. The four featured atmospheric motion categories given by SOM (Figure S8) were identified as follows:

1. Local-scale dominance (LD): average L_{bj} = 70.9 km, S_{bj} = 107.8 km, R_{bj} = 0.35, R_{std} = 0.25. This category features high R_{bj} and R_{std}. As described in section 2.5, high R_{std} indicates greater divergence of R in 12 stations due to the strong influence of local-scale turbulence and convection. L_{bj} and S_{bj} were shorter than 130km implying stagnation (Allwine and Whiteman, 1994).

2. Local-scale strong and regional-scale weak (LSRW): average L_{bj} = 106.9 km, S_{bj} = 164.8 km, R_{bj}=0.33, R_{std} = 0.23. In these circumstances, L_{bj} and S_{bj} were longer than those under LD. R_{std} was slightly lower than that in LD.

3. Local-scale weak and regional-scale strong (LWRS): average L_{bj} =159 km, S_{bj} = 183.4 km, R_{bj}=0.13, R_{std} = 0.20. As the values suggest, both R_{bj} and R_{std} were lower than those in LD and LSRW, particularly the R_{bj}. This suggests the winds veered less frequently and the differences of R found in 12 stations were smaller than the two situations above. This situation shows that the influence of the regional-scale motion was greater compared with that in the previous two categories.

4. Regional-scale dominance (RD): average L_{bj} =235.6km, S_{bj} = 246.4 km, R_{bj}= 0.05, R_{std} = 0.18. In this category, wind direction at the study site was uniform (extremely low R_{bj}) suggesting good ventilation (Allwine and Whiteman, 1994). The differences of R found in 12 stations were even smaller implying a further increased influence of regional-scale motion. The influence of regional-scale motion far outweighs the local one in this category. Therefore, this one was considered to be dominated by strong regional-scale motion.

Presented in Table 1, the SOM result showed that 40% of cases were classified into LD, 29% were classified into RD, 17% and 14% were assigned into LSRW and LWRS respectively, suggesting most winter days were greatly influenced by local-scale motion in Baoji. Under LD, average mass concentration of eBC$_{fossil}$ (3.08 ± 2.07 µg m^{-3}) and eBC$_{biomass}$ (1.52 ± 1.19 µg m^{-3}) were the highest among all four atmospheric categories noted above and over half (60% for eBC$_{biomass}$ and 55% for eBC$_{fossil}$) of the high values (75th to 100th percentile) were found under this category (Figure 3). In addition, as shown in Figure 3, the vast majority of the high values are located in the zone indicating air stagnation (S_{bj}≤ 130km, shaded yellow). The difference is that the 75th to 100th percentile eBC$_{biomass}$ tended to cluster at R_{bj} ≤ 0.2, which indicates under LD circumstances, pollution was likely coming from the same direction where the pollution sources were agglomerated. By contrast, eBC$_{fossil}$ may come from scattered locations (R_{bj} ≥ 0.4). Under LSRW, the averaged mass concentrations of eBC$_{fossil}$ and eBC$_{biomass}$ were 2.79 ± 1.73 µg m^{-3}and 1.06 ± 0.83 µg m^{-3} respectively (Table 1), both lower than those under the LD situation. When the regional scale of motion became stronger (i.e., LWRS and RD), the average mass concentration of eBC$_{fossil}$ (2.15 ± 1.62 µg m^{-3} and 1.69 ± 1.36 µg m^{-3}) and eBC$_{biomass}$ (0.86 ± 1.58 µg m^{-3} and 0.93 ± 0.72 µg m^{-3}) were lower, presumably because strong wind encourages pollutants to mix with clear air. Interestingly, 19% of total 75th to 100th percentile eBC$_{biomass}$ was found under RD and 55% of it under good ventilation (S_{bj} ≥ 250km, R_{bj} ≤ 0.2, Figure 3, shaded grey), which implies that high mass concentrations of eBC$_{biomass}$ was carried by regional-scale airflow to the site.

Atmospheric
Chemistry
and Physics
Discussions

334   Figure 4 portrays the mass concentrations of eBC$_{fossil}$ and eBC$_{biomass}$ during the daytime and night time respectively under the

335   four featured atmospheric motion categories specified earlier. As shown in Figure 4 (a) and (c), the mean values of both source-

336   specific eBCs during daytime were the highest (3.02 ± 2.12 μg m^{-3} and 1.15 ± 0.8 μg m^{-3}) under LD and the lowest (1.36 ±

337   1.00 μg m^{-3} and 0.58 ± 0.53 μg m^{-3}) under RD. Meanwhile, the average mass concentrations of both types of eBC decreased

338   with the influence of the regional scale of atmospheric motion getting stronger. This suggests that eBC pollution was apt to

339   accumulate under the dominance of local-scale motion and diffuse under the dominance of regional-scale motion during the

340   daytime. Similar to the variations in the daytime, the mean values of eBC$_{fossil}$ (3.00 ± 2.04 μg m^{-3}) and eBC$_{biomass}$ (1.76 ± 1.33

341   μg m^{-3}) under LD were also the highest during the night. However, surprisingly, unlike eBC$_{fossil}$, the mass concentrations of

342   eBC$_{biomass}$ did not decrease with the influence of regional-scale atmospheric motion enhanced. The mean value of eBC$_{biomass}$

343   under RD was the second highest (1.17 ± 0.73 μg m^{-3}). Given the nocturnal PBHL which was higher than 100m (Figure S9)

344   under RD, the nocturnal high of eBC$_{biomass}$ could be caused by transported eBC$_{biomass}$ from upwind regions to the site.

345   **3.3 Impacts of air mass directions**

346   Atmospheric motion not only influences the dispersion of pollution at a site but also can transport polluted air mass to the site

347   from far away. Air mass movement from different directions could mean the difference between no pollution and severe

348   pollution at a receptor site. To examine the impacts caused by air masses from different directions, the hourly 24h-back

349   trajectories were calculated at 100 m above the ground using the Hybrid Single-Particle Lagrangian Integrated Trajectory model

350   (Draxler and Hess, 1998). Then the trajectories were clustered by using the angle distance method to show the general

351   directional features. This method has been widely used for air mass trajectory clusters and a detailed method description can

352   be found in Wang et al. (2018). Finally, three clusters were identified (Figure S10), with 45% of total trajectories associated

353   with Cluster No.1 which originated from the north. 36% were classified as Cluster No.2 from the east direction while Cluster

354   No.3 consisted of 19% of the total trajectories and displayed an origin from southwestly direction.

355   Hourly trajectories were assigned into the four featured atmospheric motions. The varying concentrations of the source-specific

356   eBCs associated with different clusters indicate the divergent impacts of air mass direction on the pollution level at the sampling

357   site. As presented in Table 1, LD was mainly connected with the air mass from Cluster No.2 (52%) and Cluster No.1 (45%).

358   The average mass concentrations of eBC$_{fossil}$ and eBC$_{biomass}$ associated with Cluster No.1 were 2.82 ± 1.59 μg m^{-3} and 1.34 ±

359   1.07 μg m^{-3}. In comparison, Cluster No.2 was associated with a higher mean eBC$_{fossil}$ (3.2 ± 1.73 μg m^{-3}) and the highest mean

360   eBC$_{biomass}$ (1.72 ± 1.29 μg m^{-3}) among the three clusters. This could be attributed to more intensive emissions at in the eastern

361   parts of Baoji because the majority of the population of Baoji (~75%) of the total population of Baoji) is distributed located in

362   this area (http://tjj.baoji.gov.cn/art/2020/10/15/art_9233_1216737.html, accessed on 25th/9/2021, in Chinese). Several

363   highways and railways are located in the south and southwest although population is sparse with only ~4% of the total

364   population of Baoji residing in this area. Thus Cluster No.3 associated with the highest mean eBC$_{fossil}$ concentration (3.64 ±

365   0.67 μg m^{-3}) but the lowest mean eBC$_{biomass}$ (0.67 ± 0.87 μg m^{-3}). Nonetheless, it is worth noticing that only 3% of the total

366   trajectories came from this cluster.

367   Under LSRW, 56% of the trajectories were from Cluster No.1, 33% from Cluster No.2, and 11% from Cluster No.3. Although

368   the total averaged mass concentrations (Table 1) of two types of eBC showed that generally the regional-scale motion favors

369 dissipation of eBC compared with those under LD, the eBC_{fossil} (3.43 ± 1.17 µg m^{-3}) associated with Cluster No.2 and $eBC_{biomass}$

370 associated with Cluster No.3. (1 ± 0.64 µg m^{-3}) rose by 0.23 µg m^{-3} and 0.33µg m^{-3} respectively. The rise of eBC_{fossil} associated

371 with Cluster No.2 was plausibly caused by the enhanced regional influence of pollutants brought from the adjacent region.

372 According to previous studies (Wang et al., 2016; Xu et al., 2016), severe BC pollution in winter is caused by fossil fuel

373 combustion in Xi'an which is adjacent to Baoji to the east. Studies have reported that high EC emitted from biomass burning

374 was found to have originated from Sichuan Province (Wu et al., 2020; Cai et al., 2018; Huang et al., 2020) which is adjacent

375 to the southwest of Baoji. Combined with the phenomenon that the mass concentration of $eBC_{biomass}$ associated with Cluster

376 No.3 rose with the enhancement of a regional scale of motion, it is reasonable to believe that the rise of $eBC_{biomass}$ associated

377 with Cluster No.3 was likely influenced by pollution transport from the region to the southwest.

378 Under LWRS, 42% of the trajectories were from Cluster No.1., 36% from Cluster No.3, and 22% from Cluster No.2. With a

379 stronger regional scale of motion, the mean values of eBC_{fossil} and $eBC_{biomass}$ associated with all clusters were lower than those

380 under LD, except for the $eBC_{biomass}$ associated with Cluster 3 which was further increased by 0.52 µg m^{-3}. As mentioned before,

381 this rise could be caused by regional transport.

382 In the last category (RD), 41% of the trajectories were from Cluster No.1., 39% from Cluster No.3, and 20% from Cluster No.2.

383 Same as LWRS, the average mass concentration of eBC_{fossil} and $eBC_{biomass}$ associated with Cluster No.1 was only 35% and 48%

384 of the values under LD respectively. The average mass concentration of eBC_{fossil} and $eBC_{biomass}$ associated with Cluster No.2

385 was 32% and 51% of the eBC_{fossil} and $eBC_{biomass}$ under LD. As for Cluster No.3, the average mass concentration of eBC_{fossil}

386 associated with Cluster No.3 was also the lowest among all circumstances. However, interestingly, the mean value of $eBC_{biomass}$

387 associated with Cluster No.3 was highest compared with the concentration associated with Cluster No.3 under other categories.

388 Under a stronger influence of a regional scale of motion, the value of $eBC_{biomass}$ was 1.9 times as high as that under LD.

389 **3.4 Radiative effects**

390 Figure 5a shows the DREs at top of the atmosphere ($DRE_{eBC, TOA}$), surface ($DRE_{eBC, SUF}$), and the atmosphere ($DRE_{eBC, ATM}$) of

391 eBC_{fossil} and $eBC_{biomass}$. The $DRE_{eBC, TOA}$ of eBC_{fossil} ($DRE_{eBCfossil, TOA}$) and $eBC_{biomass}$ ($DRE_{eBCbiomass, TOA}$) were 9.4 ± 7.5 W m^{-2}

392 and 3.6 ± 3.4 W m^{-2} indicating a warming effect at the top of the atmosphere. The $DRE_{eBCfossil, SUF}$ ($DRE_{eBC, SUF}$ of eBC_{fossil}) and

393 $DRE_{eBCbiomass, SUF}$ ($DRE_{eBC, SUF}$ of $eBC_{biomass}$) were -6.4 ± 6.2 W m^{-2} and -16.5 ± 13.5 W m^{-2} showing a cooling effect at the

394 surface. The $DRE_{eBC, ATM}$ of eBC_{fossil} ($DRE_{eBCfossil, ATM}$) and $eBC_{biomass}$ ($DRE_{eBCbiomass, ATM}$) were 25.9 ± 20.8 W m^{-2} and 10 ± 9.5

395 W m^{-2} in the atmosphere, indicating a heating effect.

396 Figure 5 also shows the $DRE_{eBC, ATM}$ of the source-specific eBC under different featured atmosphere motions. In general, the

397 changes of $DRE_{eBC, ATM}$ are in accordance with the mass concentrations of eBC. The $DRE_{eBCfossil, ATM}$ under LD was the largest

398 with a mean value of 30.4 ± 23 W m^{-2}, followed by $DRE_{eBCfossil, ATM}$ under LSRW (28.7 ± 20.7 W m^{-2}). As the mass

399 concentration of eBC_{fossil} was lowered by a stronger regional scale of motion, the $DRE_{eBC, ATM}$ under LWRS and RD were also

400 lower compared with those in LD and LSRW. By contrast, the $DRE_{eBC, ATM}$ of $eBC_{biomass}$ under LSRW was the highest (11.5 ±

401 11.8 W m^{-2}), though it is only 0.3 W m^{-2} higher than that under LD, which could be caused by the higher max value and higher

402 75th percentile in day time (Figure 4). When the regional scale of motion became stronger, the $DRE_{eBCbiomass, ATM}$ declined as

403   expected due to the lowered mass concentration. The $DRE_{eBC, ATM}$ of $eBC_{biomass}$ under LWRS and RD were 8.6 ± 8.5 W m^{-2} and

404   7.9 ± 7.4 W m^{-2} respectively.

405   Although $DRE_{eBC, ATM}$ declined with increased influence from the regional scale of motion, the $DRE_{eBC, ATM}$ efficiency ($DRE_{eBC,}$

406    $_{ATM}$ per mass concentration) was found to increase with the enhancement of regional-scale motion. The calculation showed that

407   DRE efficiencies of both types of eBC under LD and LSRW were comparable, which were around 10 W m^{-2} (Table 2). In

408   contrast, efficiencies varied more so under a stronger influence of regional-scale motion. Under LWRS, the efficiencies of

409   eBC_{fossil} and $eBC_{biomass}$ were 13.5 ± 6.7 (W m^{-2})/(μg m^{-3}) and 14.7 ± 8.1 (W m^{-2})/(μg m^{-3}) respectively. Under RD, the

410   efficiencies were even higher, which were 15.6 ± 8.9 (W m^{-2})/(μg m^{-3}) and 15.5 ± 6.7 (W m^{-2})/(μg m^{-3}) respectively, over 1.5

411   times those recorded under LD. Studies have confirmed that the aging processes in the atmosphere would enhance the light-

412   absorbing ability of BC (Chen et al., 2017; Shen et al., 2014), and regional transport can provide sufficient time for BC aging

413   (Shiraiwa, et al. 2007; Cho et al., 2021). Therefore, the disproportional change between mass concentration and DRE efficiency

414   was very likely caused by the strong regional-scale motion that blew away the fresh BC from local emissions but in the

415   meantime brought in aged BC from the upwind regions. As a result, the transported BC reached a receptor site with a higher

416   light-absorbing ability which led to a higher DRE efficiency of BC at the sampling site when regional scale motion is strong.

417   This strongly implies a greater perturbation to regional climate caused by the regionally transported BC, particularly in the

418   river-valley city due to weak dispersion conditions (Zhao et al., 2015; Wang et al., 2013) indicating a potentially enhanced

419   climatic effect.

420   **4 Conclusions**

421   This study derived site-specific AAEs using the PMF model with chemical and optical data collected in a river-valley city

422   during winter. With those AAEs, source-specific eBCs (i.e., eBC_{fossil} and $eBC_{biomass}$) were then apportioned using the

423   aethalometer model. Finally, the impacts of different featured atmospheric motions on the mass concentrations of the source-

424   specific eBCs and the induced DREs were investigated. The result showed that four sources of eBC were identified, that is

425   diesel vehicular emissions, biomass burning, coal combustion, and mineral dust. The derived AAEs were 1.07 for diesel

426   vehicular emissions, 2.13 for biomass burning, 1.74 for coal combustion, and 1.78 for mineral dust. The mean values of eBC_{fossil}

427   and $eBC_{biomass}$ were 2.46 μg m^{-3} and 1.17 μg m^{-3} respectively.

428   During the sampling period, the mass concentrations of source-specific eBC were influenced by four featured atmospheric

429   motions identified by SOM. Amongst those motions, the local-scale motion played an important role on most winter days. The

430   eBC_{fossil} and $eBC_{biomass}$ under those identified featured atmospheric motions showed that over half (60% for $eBC_{biomass}$ and 55%

431   for eBC_{fossil}) of high values (75th to 100th percentile) were found under LD. This illustrates that the BC pollution in general was

432   more likely to happen when the influence from local-scale motion outweighed from regional-scale motion. However, although

433   regional-scale motion generally lowered eBCs, 19% of the high values of $eBC_{biomass}$ were still found under RD, particularly

434   under good ventilation. Furthermore, the air mass from different directions also posted divergent impacts on the source-specific

435   eBCs under different motions. eBC_{fossil} most likely accumulated under a stronger influence of local-scale motion, by contrast

Atmospheric
Chemistry
and Physics
Discussions

436   besides accumulating under a strong local-scale motion, eBC$_{biomass}$ was also found raised continuously with the enhanced

437   regional scale of motion when the air masses from the southwest, indicating an evident regional transport.

438   Similar to the mass concentrations, the DREs of the two types of eBC were both lower when the regional scale of motion

439   outweighed the local one. However, the changes of mass concentration and DREs were disproportional because the regional-

440   scale of motion blew the fresh BC away from the local site but carried the aged BCs from the upwind regions. As a result, the

441   DRE efficiency of eBC was ~1.5 times higher when the regional scale of motion was stronger. This study revealed that the

442   divergent influence of different scales of air motions on the mass concentrations of source-specific eBCs and their DRE

443   efficiencies. It highlights that the DRE efficiency of BC was enhanced during regional transport which could lead to greater

444   consequences in receptor regions and the potential enhanced climatic effect of regionally transported BC is worthy of attention

445   in terms of regional climate stability.

446   *Data availability*. The data are available from the authors upon request.

447   *Supplement*. The supplement related to this article is available online.

448   *Author contributions*. QW and JC designed the study. BZ and SL conducted the field measurements. YQ and JT conducted
449   data analysis. SL and TZ performed the chemical analysis of filters. HL draft the article and QW revised it. JC and YH
450   commented on the paper.

451   *Competing interests*. The authors declare that they have no conflict of interest.

455   **Reference**

456   Amato, F., Alastuey, A., Karanasiou, A., Lucarelli, F., Nava, S., Calzolai, G., Severi, M., Becagli, S., Gianelle, V. L., Colombi,
457   C., Alves, C., Custódio, D., Nunes, T., Cerqueira, M., Pio, C., Eleftheriadis, K., Diapouli, E., Reche, C., Minguillón, M.
458   C., Manousakas, M.-I., Maggos, T., Vratolis, S., Harrison, R. M., and Querol, X.: AIRUSE-LIFE+: a harmonized PM
459   speciation and source apportionment in five southern European cities, Atmos. Chem. Phys., 16, 3289–3309,
460   https://doi.org/10.5194/acp-16-3289-2016, 2016.

461   Artaxo, P., Fernandas, E. T., Martins, J. V., Yamasoe, M. A., Maenhaut, W., Longo, K. M., Castanho, A., and Hobbs, P. V.:
462   Large-scale aerosol source apportionment in Amazonia, J. Geophys. Res.-Atmos., 103, 31837–31847,
463   https://doi.org/10.1029/98jd02346, 1998.

464   Allwine, K. J., and Whiteman, C. D.: Single-station integral measures of atmospheric stagnation, recirculation and ventilation.
465   Atmos. Environ., 28: 713–721, https://doi.org/10.1016/1352-2310(94)90048-5, 1994.

466   Bond, T. C., Doherty, S. J., Fahey, D. W., Forster, P. M., Berntsen, T., DeAngelo, B. J., Flanner, M. G., Ghan, S., Karcher, B.,
467   Koch, D., Kinne, S., Kondo, Y., Quinn, P. K., Sarofim, M. C., Schultz, M. G., Schulz, M., Venkataraman, C., Zhang, H.,
468   Zhang, S., Bellouin, N., Guttikunda, S. K., Hopke, P. K., Jacobson, M. Z., Kaiser, J. W., Klimont, Z., Lohmann, U.,
469   Schwarz, J. P., Shindell, D., Storelvmo, T., Warren, S. G., and Zender, C. S.: Bounding the role of black carbon in the
470   climate system: A scientific assessment, J. Geophys. Res.-Atmos., 118, 5380–5552, https://doi.org/10.1002/jgrd.50171,
471   2013.

472   Brulfert, G., Chemel, C., Chaxel, E., Chollet, J., Jouve, B., and Villard, H.: Assessment of 2010 air quality in two Alpine valleys
473   from modelling: Weather type and emission scenarios, Atmos. Environ., 40, 7893–7907,
474   https://doi.org/10.1016/j.atmosenv.2006.07.021, 2006.

475 Cao, J. J., Zhu, C. S., Tie, X. X., Geng, F. H., Xu, H. M., Ho, S. S. H., Wang, G. H., Han, Y. M., and Ho, K. F.: Characteristics
476   and sources of carbonaceous aerosols from Shanghai, China, Atmos. Chem. Phys., 13, 803-817,
477   https://doi.org/10.5194/acp-13-803-2013, 2013.

478 Cai, S., Ma, Q., Wang, S., Zhao, B., Brauer, M., Cohen, A., Martin, R., Zhang, Q., Li, Q., Wang, Y., Hao, J., Frostad, J.,
479   Forouzanfar, M., and Burnett, R.: Impact of air pollution control policies on future PM2.5 concentrations and their source
480   contributions in China, J. Environ. Manage., 227, 124–133, https://doi.org/10.1016/j.jenvman.2018.08.052, 2018.

481 Cappa, C. D., Onasch, T. B., Massoli, P., Worsnop, D. R., Bates, T. S., Cross, E. S., Davidovits, P., Hakala, J., Hayden, K. L.,
482   Jobson, B. T., Kolesar, K. R., Lack, D. A., Lerner, B. M., Li, S.-M., Mellon, D., Nuaaman, I., Olfert, J. S., Petäjä, T.,
483   Quinn, P. K., Song, C., Subramanian, R., Williams, E. J., and Zaveri, R. A.: Radiative Absorption Enhancements Due to
484   the Mixing State of Atmospheric Black Carbon, Science., 337, 1078–1081, https://doi.org/10.1126/science.1223447, 2012.

485 Carvalho, A.C., Carvalho, A., Gelpi, I., Barreiro, M., Borrego, C., Miranda, A., and Perez-Munuzuri, V.: Influence of
486   topography and land use on pollutants dispersion in the Atlantic coast of Iberian Peninsula, Atmos. Environ., 40,3969–
487   3982, https://doi.org/10.1016/j.atmosenv.2006.02.014, 2006.

488 Cho, C., Schwarz, J., Perriing, A., Lamb, K., Kondo, Y., Park, J., Park, D., Shim, K., Park, J., Park, R., Lee, M., Song, C., Kim,
489   S.: Light-absorption enhancement of black carbon in the Asian outflow inferred from airborne SP2 and in-situ
490   measurements during KORUS- AQ, Sci. Total Environ., 773, 145531, https://doi.org/10.1016/j.scitotenv.2021.145531,
491   2021.

492 Cheng, Y., He, K., Zheng, M., Duan, F., Ma, Y., Tan, J., Yang, F., Liu, J., Zhang, X., Weber, R., Bergin, M. and Russell, A.:
493   Mass absorption efficiency of elemental carbon and water-soluble organic carbon in Beijing, China, Atmos. Chem. Phys.,
494   11, 11497–11510, https://doi:10.5194/acp-11-11497-2011, 2011.

495 Chen, X., Wang, Z., Yu, F., Pan, X., Li, J., Ge, B., Wang, Z., Hu, M., Yang, W., Chen, H.: Estimation of atmospheric aging
496   time of black carbon particles in the polluted atmosphere over central-eastern China using microphysical process analysis
497   in regional chemical transport model, Atmos. Environ., 163,44-56, https://doi.org/10.1016/j.atmosenv.2017.05.016, 2017

498 Drinovec, L., Močnik, G., Zotter, P., Prévôt, A. S. H., Ruckstuhl, C., Coz, E., Rupakheti, M., Sciare, J., Müller, T.,
499   Wiedensohler, A., and Hansen, A. D. A.: The "dual-spot" Aethalometer: an improved measurement of aerosol black
500   carbon with real-time loading compensation, Atmos. Meas. Tech., 8, 1965-1979, https://doi.org/10.5194/amt-8-1965-2015,
501   2015.

502 Draxler, R., and Hess, G.: An overview of the HYSPLIT_4 modelling system for trajectories, Aust. Meteorol. Mag., 47, 1998.

503 Dutton, J., The Ceaseless Wind an Introduction to The Theory of Atmospheric Motion, McGraw-Hill, Inc., U.S.A., 1976

504 Geivanidis, S., Pistikopoulos, P., and Samaras, Z.: Effect on exhaust emissions by the use of methylcyclopentadienyl
505   manganese tricarbonyl (MMT) fuel additive and other lead replacement gasolines. Sci. Total Environ., *305*, 129-141,
506   https://doi.org/10.1016/S0048-9697(02)00476-X, 2003.

507 Green, M., Chow, J., and Watson, G.: Effects of Snow Cover and Atmospheric Stability on Winter PM2.5 Concentrations in
508   Western U.S. Valleys, Journal of Applied Meteorology and Climatology., 54, https://doi.org/doi: 10.1175/JAMC-D-14-
509   0191.1, 2016.

510 Han, H., Liu, J., Shu, L., Wang, T., and Yuan, H.: Local and synoptic meteorological influences on daily variability in
511   summertime surface ozone in eastern China, Atmos. Chem. Phys., 20, 203–222, https://doi.org/10.5194/acp-20-203-2020,
512   2020.

513 Helin, A., Niemi, J. V., Virkkula, A., Pirjola, L., Teinilä, K., Backman, J., Aurela, M., Saarikoski, S., Rönkkö, T., Asmi, E.,
514   and Timonen, H.: Characteristics and source apportionment of black carbon in the Helsinki metropolitan area, Finland,
515   Atmos. Environ., 190, 87-98, https://doi.org/10.1016/j.atmosenv.2018.07.022, 2018.

516 He, C., Liou, K.-N., Takano, Y., Zhang, R., Levy Zamora, M., Yang, P., Li, Q., and Leung, L. R.: Variation of the radiative
517   properties during black carbon aging: theoretical and experimental intercomparison, Atmos. Chem. Phys., 15, 11967–
518   11980, https://doi.org/10.5194/acp-15-11967-2015, 2015.

519 Hewitson, B. C. and Crane, R. G.: Consensus between GCM climate change projections with empirical downscaling:
520   precipitation downscaling over South Africa, Int. J. Climatol., 26, 1315–1337, https://doi.org/10.1002/joc.1314, 2006.

Atmospheric
Chemistry
and Physics
Discussions

521 Hsu, C.-Y., Chiang, H.-C., Lin, S.-L., Chen, M.-J., Lin, T.-Y., and Chen, Y.-C.: Elemental characterization and source
522   apportionment of PM 10 and PM 2.5 in the western coastal area of central Taiwan, Sci. Total Environ., 541, 1139-1150,
523   https://doi.org/10.1016/j.scitotenv.2015.09.122, 2016.

524 Huang, Y., Zhang, L., Li, T., Chen, Y., and Yang, F.: Seasonal Variation of Carbonaceous Species of $PM_{2.5}$ in a Small City in
525   Sichuan Basin, China, Atmosphere., 11, 1286, https://doi.org/10.3390/atmos11121286, 2020.

526 Jacobson, M. Z.: Control of fossil-fuel particulate black carbon and organic matter, possibly the most effective method of
527   slowing global warming, J. Geophys. Res., 107, 4410, https://doi.org/10.1029/2001JD001376, 2002.

528 Jiang, N. B., Scorgie, Y., Hart, M., Riley, M. L., Crawford, J., Beggs, P. J., Edwards, G. C., Chang, L. S., Salter, D., and
529   Virgilio, G. D.: Visualising the relationships between synoptic circulation type and air quality in Sydney, a subtropical
530   coastal-basin environment, Int. J. Climatol., 37, 1211–1228, https://doi.org/10.1002/joc.4770, 2017.

531 Kahnert, M., and Kanngiesser, F.: Review: modelling optical properties of atmospheric black carbon aerosols. J. Quant.
532   Spectrosc., RA, 244, 106849, https://doi.org/10.1016/j.jqsrt.2020.106849, 2020.

533 Kalthoff, N., Horlacher, V., Corsmeier, U., Volz-Thomas, A., Kolahgar, B., Geiß, H., Möllmann-Coers, M., and Knaps, A.:
534   Influence of valley winds on transport and dispersion of airborne pollutants in the Freiburg-Schauinsland area, J. Geophys.
535   Res.-Atmos., 105, 1585–1597, https://doi.org/10.1029/1999jd900999, 2000.

536 Kirchstetter, T. W., Novakov, T., and Hobbs, P. V.: Evidence that the spectral dependence of light absorption by aerosols is
537   affected by organic carbon, J. Geophys. Res.-Atmos., 109, D21208, https://doi.org/10.1029/2004jd004999, 2004.

538 Kohonen, T.: The self-organizing map, Proc. IEEE, 78, 1464–1480, https://doi.org/10.1109/5.58325, 1990.

539 Liao, Z., Xie, J., Fang, X., Wang, Y., Zhang, Y., Xu, X., and Fan, S.: Modulation of synoptic circulation to dry season $PM_{2.5}$
540   pollution over the Pearl River Delta region: An investigation based on self-organizing maps. Atmos. Environ., 230, 117482,
541   https://doi.org/10.1016/j.atmosenv.2020.117482, 2020.

542 Lewis, C. W., Norris, G. A., Conner, T. L., and Henry, R. C.: Source apportionment of Phoenix PM2.5 aerosol with the Unmix
543   receptor model, J. Air Waste Manage., 53, 325–338, https://doi.org/10.1080/10473289.2003.10466155, 2003.

544 Levy, I., Dayan, U., and Mahrer, Y.: Differing atmospheric scales of motion and their impact on air pollutants, Int. J. Climatol.,
545   30, 612–619, https://doi.org/10.1002/joc.1905, 2010.

546 Lin, Y., Tsai, C., Wu, T., Zhang, R., Chi, K., Huang, Y., Lin, S., and Hsu, S.: Characteristics of trace metals in traffic-derived
547   particles in Hsuehshan Tunnel, Taiwan: size distribution, potential source, and fingerprinting metal ratio, Atmos. Chem.
548   Phys., 15, 4117–4130, https://doi.org/10.5194/acp-15-4117-2015, 2015.

549 IPCC: Climate Change 2021: The Physical Science Basis. Contribution of Working Group I to the Sixth Assessment Report of
550   the Intergovernmental Panel on Climate Change [Masson-Delmotte, V., P. Zhai, A. Pirani, S.L. Connors, C. Péan, S.
551   Berger, N. Caud, Y. Chen, L. Goldfarb, M.I. Gomis, M. (eds)], https://reliefweb.int/report/world/climate-change-2021-
552   physical-science-basis, 2021

553 Manousakas, M., Papaefthymiou, H., Diapouli E., Migliori, A., Karydas, A.G., Bogdanovic-Radovic, I., Eleftheriadis, K.:
554   Assessment of PM2.5 sources and their corresponding level of uncertainty in a coastal urban area using EPA PMF 5.0
555   enhanced diagnostics, Sci. Total Environ., 574, 155–164, https://doi.org/10.1016/j.scitotenv.2016.09.047, 2017.

556 Manö, S., and Andreae, M.O.: Emission of methyl bromide from biomass burning. Science., 263, 1255–1257,
557   https://doi.org/10.1126/science.263.5151.1255, 1994.

558 Norris, G., Duvall, R., Brown, S. and Bai, S.: EPA Positive Matrix Factorization (PMF) 5.0 fundamentals and User Guide
559   Prepared for the US Environmental Protection Agency Office of 30 Research and Development, Washington, DC, by the
560   National Exposure Research Laboratory, Research Triangle Park; Sonoma Technology, Inc., Petaluma.,
561   https://www.epa.gov/air-research/epa-positive-matrix-factorization-50-fundamentals-and-user-guide, 2014.

562 Ochoa-Hueso, R., Munzi, S., Alonso, R., Arróniz-Crespo, M., Avila, A., Bermejo, V., Bobbink, R., Branquinho, C.,
563   Concostrina-Zubiri, L., Cruz, C., Cruz de Carvalho, R., De Marco, A., Dias, T., Elustondo, D., Elvira, S., Estébanez, B.,
564   Fusaro, L., Gerosa, G., Izquieta-Rojano ,S., Lo Cascio, M., Marzuoli, R., Matos, P., Mereu, S., Merino, J., Morillas, L.,
565   Nunes, A., Paoletti, E., Paoli, L., Pinho, P., Rogers, I.B., Santos, A., Sicard, P., Stevens, C. J., and Theobald, M. R.:

566 Ecological impacts of atmospheric pollution and interactions with climate change in terrestrial ecosystems of the
567 Mediterranean Basin: Current research and future directions, Environ. Pollut., 227, 194–206, 2017.

568 Oke, T., Boundary Layer Climates, 2nd edition, Taylor & Francis e-Library, 2002.

569 Pathak, B., Kalita, G., Bhuyan, K., Bhuyan, P. and Moorthy, K.: Aerosol Temporal Characteristics and Its Impact on Shortwave
570 Radiative Forcing at A Location in The Northeast of India, J. Geophys. Res.-Atmos., 115, D19204,
571 https://doi:10.1029/2009JD013462, 2010.

572 Peng, J., Hu, M., Guo, S., Du, Z., Zheng, J., Shang, D., Levy, M., and Zeng, L.: Markedly enhanced absorption and direct
573 radiative forcing of black carbon under polluted urban environments, P. Natl. Acad. Sci. USA, 113, 4266–4271,
574 https://doi.org/10.1073/pnas.1602310113, 2016.

575 Pearce, J. L., Waller, L. A., Chang, H. H., Klein, M., Mulholland, J. A., Sarnat, J. A., Sarnat, S. E., Strickland, M. J., and
576 Tolbert, P. E.: Using self-organizing maps to develop ambient air quality classifications: a time series example, Environ.
577 Health-Glob., 13, https://doi.org/10.1186/1476-069X-13-56, 2014.

578 Rajesh, T. A., and Ramachandran, S.: Black carbon aerosols over urban and high altitude remote regions: Characteristics and
579 radiative implications, Atmos. Environ., 194, 110-122, https://doi.org/10.1016/j.atmosenv.2018.09.023, 2018.

580 Reusch, D.B., Alley, R.B., and Hewitson, B.C.: Relative performance of Self-Organizing Maps and Principal Component
581 Analysis in pattern extraction from synthetic climatological data. Polar Geogr., 29(3): 188–212.
582 http://dx.doi.org/10.1080/789610199, 2005.

583 Ricchiazzi, P., Yang, S., Gautier, C., and Sowle, D.: SBDART: A research and teaching software tool for plane-parallel
584 radiative transfer in the Earth's atmosphere, B. Am. Meteorol. Soc., 79, 2101–2114, https://doi.org/10.1175/1520-
585 0477(1998)0792.0.CO;2, 1998.

586 Sandradewi, J., Prévôt, A. S. H., Weingartner, E., Schmidhauser, R., Gysel, M., and Baltensperger, U.: A study of wood burning
587 and traffic aerosols in an Alpine valley using a multi-wavelength Aethalometer, Atmos. Environ., 42, 101-112,
588 https://doi.org/10.1016/j.atmosenv.2007.09.034, 2008.

589 Seinfeld, J., and Pandis, S., 2006. Atmospheric chemistry and physics: from air pollution to climate change, 2nd ed., Published
590 by John Wiley & Sons, Inc., Hoboken, New Jersey, United States of America,

591 Schroter, D., Cramer, W., Leemans, R., Prentice, C., Araujo, M., Arnell, N., Bondeau, A., Bugmann, H., Carter, T., Gracia, C.,
592 de la Vega-Leinert, A., Erhard, M., Ewert, F., Glendining, M., House, J., Kankaanpaa, S., Klein, R., Lavorel, S., Lindner,
593 M., Metzger, M., Meyer, J., Mitchell, T., Reginster, I., Rounsevell, M., Sabate, S., Sitch, S., Smith, B., Smith, J., Smith,
594 P., Sykes, ´M., Thonicke, K., Thuiller, W., Tuck, G., Zaehle, S., and Zierl, B.: Ecosystem service supply and vulnerability
595 to Global Change in Europe, Science., 310, 1333–1337, https://doi.org/10.1126/science.1115233, 2005.

596 Shen, Z., Liu, J., Horowitz, W., Henze, D., Levy, H., Mauzerall, D., Lin, J., and Tao, S.: Analysis of transpacific transport of
597 black carbon during HIPPO-3: implications for black carbon aging, Atmos. Chem. Phys., 14, 6315–6327,
598 https://doi.org/10.5194/acp-14-6315-2014, 2014.

599 Shiraiwa, M., Kondo, Y., Moteki, N., Takegawa, N., Miyazaki, Y., and Blake, D. R.: Evolution of Mixing State of Black
600 Carbon in Polluted Air from Tokyo, Geophys. Res. Letters., 34, L16803, https://doi.org/10.1029/2007GL029819, 2007.

601 Shindell, D., Kuylenstierna, J. C. I., Vignati, E., van Dingenen, R., Amann, M., Klimont, Z., Anenberg, S. C., Muller, N.,
602 JanssensMaenhout, G., Raes, F., Schwartz, J., Faluvegi, G., Pozzoli, L., Kupiainen, K., Hoglund-Isaksson, L., Emberson,
603 L., Streets, D., Ramanathan, V., Hicks, K., Oanh, N. T. K., Milly, G., Williams, M., Demkine, V., and Fowler, D.:
604 Simultaneously Mitigating Near-Term Climate Change and Improving Human Health and Food Security, Science, 335,
605 183–189, https://doi.org/10.1126/science.1210026, 2012.

606 Song, Y., Zhang, Y., Xie, S., Zeng, L., Zheng, M., Salmon, L. G., Shao, M., and Slanina, S.: Source apportionment of PM2.5
607 in Beijing by positive matrix factorization, Atmos. Environ., 40, 1526-1537,
608 https://doi.org/10.1016/j.atmosenv.2005.10.039, 2006.

609 Sun, J., Zhi, G., Hitzenberger, R., Chen, Y., Tian, C., Zhang, Y., Feng, Y., Cheng, M., Zhang, Y., Cai, J., Chen, F., Qiu, Y.,
610 Jiang, Z., Li, J., Zhang, G., and Mo, Y.: Emission factors and light absorption properties of brown carbon from household
611 coal combustion in China, Atmos. Chem. Phys., 17, 4769–4780, https://doi.org/10.5194/acp-17-4769-2017, 2017.

612 Stauffer, R. M., Thompson, A. M., and Young, G. S.: Tropospheric ozonesonde profiles at long-term US monitoring sites: 1.
613   A climatology based on self-organizing maps, J. Geophys. Res.-Atmos, 121, 1320–1339,
614   https://doi.org/10.1002/2015JD023641, 2016.

615 Tan, J., Zhang, L. Zhou, X., Duan, J. Li, Y., Hu, J., and He, K.: Chemical characteristics and source apportionment of PM2.5
616   in Lanzhou, China, Sci. Total Environ., 601, 1743-1752, https://doi.org/10.1016/j.scitotenv.2017.06.050, 2017.

617 Tao, J., Zhang L., Zhang, R., Wu, Y., Zhang, Z., Zhang, X., Tang. Y., Cao, J., and Zhang, Y.: Uncertainty assessment of source
618   attribution of PM2.5 and its water-soluble organic carbon content using different biomass burning tracers in positive
619   matrix factorization analysis — a case study in Beijing, China, Sci. Total Environ., 543, 326–335,
620   https://doi.org/10.1016/j.scitotenv.2015.11.057, 2016.

621 Tao, J., Zhang, L. M., Cao, J. J., Zhong, L. J., Chen, D. S., Yang, Y. H., Chen, D. H., Chen, L. G., Zhang, Z. S., Wu, Y. F.,
622   Xia, Y. J., Ye, S. Q., and Zhang, R. J.: Source apportionment of PM2.5 at urban and suburban areas of the Pearl River
623   Delta region, south China – with emphasis on ship emissions, Sci. Total Environ., 574, 1559–1570,
624   https://doi.org/10.1016/j.scitotenv.2016.08.175, 2017.

625 Thorpe, A., and Harrison, R. M.: Sources and properties of non-exhaust particulate matter from road traffic: A review, Sci.
626   Total Environ., *400*, 270-282, https://doi.org/10.1016/j.scitotenv.2008.06.007, 2008.

627 Urban, R. C., Lima-Souza, M., Caetano-Silva, L., Queiroz, M. E. C., Nogueira, R. F. P., Allen, A. G., Cardoso, A. A., Held,
628   G., and Campos, M. L. A. M.: Use of levoglucosan, potassium, and water-soluble organic carbon to characterize the
629   origins of biomass-burning aerosols, Atmos. Environ., 61, 562-569, https://doi.org/10.1016/j.atmosenv.2012.07.082, 2012.

630 Wang, Q., Cao, J., Han, Y., Tian, J., Zhu, C., Zhang, Y., Zhang, N., Shen, Z., Ni, H., Zhao, S., and Wu, J.: Sources and
631   physicochemical characteristics of black carbon aerosol from the southeastern Tibetan Plateau: internal mixing enhances
632   light absorption, Atmos. Chem. Phys., 18, 4639-4656, https://doi.org/10.5194/acp-18-4639-2018, 2018.

633 Wang, Q., Huang, R., Zhao, Z., Cao, J., Ni, H., Tie, X., Zhao, S., Su, X., Han, Y., Shen, Z., Wang, Y., Zhang, N., Zhou, Y.,
634   and Corbin, J.: Physicochemical characteristics of black carbon aerosol and its radiative impact in a polluted urban area
635   of China, J. Geophys. Res. Atmos., 121, https://doi.org/doi:10.1002/2016JD024748, 2016.

636 Wang, Q., Han, Y., Ye, J., Liu, S., Pongpiachan, S., Zhang, N., Han, Y., Tian, J., Wu, C., Long, X., Zhang, Q., Zhang, W.,
637   Zhao, Z., and Cao, J.: High contribution of secondary brown carbon to aerosol light absorption in the southeastern margin
638   of Tibetan Plateau, Geophys. Res. Lett., 46, 4962–4970, https://doi.org/10.1029/2019GL082731, 2019.

639 Wang, Q., Liu, H., Wang, P., Dai, W., Zhang T., Zhao, Y., Tian, J., Zhang, W., Han, Y., and Cao, J.: Optical source
640   apportionment and radiative effect of light-absorbing carbonaceous aerosols in a tropical marine monsoon climate zone:
641   the importance of ship emissions, Atmos. Chem. Phys., 20, 15537–15549, https://doi.org/10.5194/acp-20-15537-2020,
642   2020.

643 Wang, W., Chen, N., and Ma, X., , Characteristic Analysis on Mountain-valley Wind in Deep valley, Advanced Materials
644   Research, Vols 610-613, pp 817-824, https://doi:10.4028/www.scientific.net/AMR.610-613.817, 2013.

645 Wei, N., Wang, N., Huang, X., Liu, P., and Chen, L.: The effects of terrain and atmospheric dynamics on cold season heavy
646   haze in the Guanzhong Basin of China, Atmos. Pollut. Res., 11, 1805-1819, https://doi.org/10.1016/j.apr.2020.07.007,
647   2020.

648 Wu, J., Kong, S., Wu, F., Cheng, Y., Zheng, S., Qin, S., Liu, X., Yan, Q., Zheng, H., Zheng, M., Yan, Y., Liu, D., Ding, S.,
649   Zhao, D., Shen, G., Zhao, T., and Qi, S.: The moving of high emission for biomass burning in China: View from multiyear
650   emission estimation and human-driven forces, Environ. Int., 142, 105812, https://doi.org/10.1016/j.envint.2020.105812,
651   2020.

652 Wu, C. and Yu, J. Z.: Determination of primary combustion source organic carbon-to-elemental carbon (OC / EC) ratio using
653   ambient OC and EC measurements: secondary OC-EC correlation minimization method, Atmos. Chem. Phys., 16, 5453–
654   5465, https://doi.org/10.5194/acp-16-5453-2016, 2016.

655 Xu, H. M., Cao, J. J., Ho, K. F., Ding, H., Han, Y. M., Wang, G. H., Chow, J. C., Watson, J. G., Khol, S. D., Qiang, J., and Li,
656   W. T.: Lead concentrations in fine particulate matter after the phasing out of leaded gasoline in Xi'an, China, Atmos.
657   Environ., 46, 217– 224, https://doi.org/10.1016/j.atmosenv.2011.09.078, 2012.

658   Xu, H., Ren, Y., Zhang, W., Meng,W., Yun, X., Yu, X., Li, J., Zhang, Y., Shen, G., Ma, J., Li, B., Cheng, H., Wang, X., Wan,
659   Y., and Tao, S.: Updated Global Black Carbon Emissions from 1960 to 2017: Improvements, Trends, and Drivers, Environ.
660   Sci. Technol., 55, 7869-7879, https://doi.org/10.1021/acs.est.1c03117, 2021.

661   Xu, H., Cao, J., Chow, J., Huang, R., Shen, Z., Chen, L.W., Ho, K., Watson, J.: Inter-annual variability of wintertime PM2.5
662   chemical composition in Xi'an, China: Evidences of changing source emissions, Sci. Total Environ., 545, 546–555,
663   http://dx.doi.org/10.1016/j.scitotenv.2015.12.070, 2016.

664   Yang, M., Howell, S. G., Zhuang, J., and Huebert, B. J.: Attribution of aerosol light absorption to black carbon, brown carbon,
665   and dust in China – interpretations of atmospheric measurements during EAST-AIRE, Atmos. Chem. Phys., 9, 2035–2050,
666   https://doi.org/10.5194/acp-9-2035-2009, 2009.

667   Yao, X., Chan, C. K., Fang, M., Cadle, S., Chan, T., Mulawa, P., He, K., and Ye, B.: The water-soluble ionic composition of
668   PM2.5 in Shanghai and Beijing, China, Atmos. Environ., 36, 4223–4234, https://doi.org/10.1016/S1352-2310(02)00342-
669   4, 2002.

670   Zhao, S., Tian, H., Luo, L., Liu, H., Wu, B., Liu, S., Bai, X., Liu, W., Liu, X., Wu, Y., Lin, S., Guo, Z., Lv, Y., and Xue, Y.:
671   Temporal variation characteristics and source apportionment of metal elements in PM2.5 in urban Beijing during 2018–
672   2019, Environ. Pollut., 268, 115856, https://doi.org/10.1016/j.envpol.2020.115856, 2021.

673   Zhao, S., Tie, X., Cao, J., and Zhang, Q.: Impacts of mountains on black carbon aerosol under different synoptic meteorology
674   conditions   in   the   Guanzhong   region,   China,   Atmos.   Res.,   164–165,   286–296,
675   https://doi.org/10.1016/j.atmosres.2015.05.016, 2015

676   Zhao, S. P., Yu, Y., Yin, D., Yu, Z., Dong, L. X., Mao, Z., He, J. J., Yang, J., Li, P., and Qin, D. H.: Concentrations, optical
677   and radiative properties of carbonaceous aerosols over urban Lanzhou, a typical valley city: Results from in-situ
678   observations and numerical model, Atmos. Environ., 213, 470–484, https://doi.org/10.1016/j.atmosenv.2019.06.046, 2019.

679   Zhang, Z., Gao, J., Engling, G., Tao, J., Chai, F., Zhang, L., Zhang, R., Sang, X., Chan, C., Lin, Z., and Cao, J.: Characteristics
680   and applications of size-segregated biomass burning tracers in China's Pearl River Delta region, Atmos. Environ., 102,
681   290–301. https://doi.org/10.1016/j.atmosenv.2014.12.009, 2015.

682   Zhang, J. P., Zhu, T., Zhang, Q. H., Li, C. C., Shu, H. L., Ying, Y., Dai, Z. P., Wang, X., Liu, X. Y., Liang, A. M., Shen, H.
683   X., and Yi, B. Q.: The impact of circulation patterns on regional transport pathways and air quality over Beijing and its
684   surroundings, Atmos. Chem. Phys., 12, 5031–5053, https://doi.org/10.5194/acp-12-5031-2012, 2012.

685   Zhang, Y., Li, M., Cheng, Y., Geng, G., Hong, C., Li, H., Li, X., Tong, D., Wu, N., Zhang, X., Zheng, B., Zheng, Y., Bo, Y.,
686   Su, H., and Zhang, Q.: Modeling the aging process of black carbon during atmospheric transport using a new approach: a
687   case study in Beijing, Atmos. Chem. Phys., 19, 9663–9680, https://doi.org/10.5194/acp-19-9663-2019, 2019.

688   Zotter, P., Herich, H., Gysel, M., El-Haddad, I., Zhang, Y., Močnik, G., Hüglin, C., Baltensperger, U., Szidat, S., and Prévôt,
689   A. S. H.: Evaluation of the absorption Ångström exponents for traffic and wood burning in the Aethalometer-based source
690   apportionment using radiocarbon measurements of ambient aerosol, Atmos. Chem. Phys., 17, 4229–4249,
691   https://doi.org/10.5194/acp-17-4229-2017, 2017

Table 1. The mass concentration of eBC from fossil fuel combustion (eBC_{fossil}) and eBC from biomass burning ($eBC_{biomass}$) associated with different clusters under four featured atmospheric motions

	Local scale dominance (LD) (40%)				Local scale strong and regional scale weak (LSRW) (17%)				Local scale weak and regional scale strong (LWRS) (14%)				Regional scale dominance (RD) (29%)			
	cluster 1	cluster 2	cluster 3	Total average	cluster 1	cluster 2	cluster 3	Total average	cluster 1	cluster 2	cluster 3	Total average	cluster 1	cluster 2	cluster 3	Total average
Trajectory percentage	45%	52%	3%		56%	33%	11%		42%	22%	36%		41%	20%	39%	
eBC_{fossil} (µg m^{-3})[a]	2.82± 1.59	3.2± 1.73	3.64± 0.67	3.08± 2.07	2.42± 1.00	3.43± 1.17	2.89± 1.00	2.79± 1.73	1.32± 0.67	2.02± 0.73	3.16± 1.19	2.15± 1.62	1.00± 0.64	1.02± 0.88	2.75± 1.26	1.69± 1.36
$eBC_{biomass}$ (µg m^{-3})[b]	1.34± 1.07	1.72± 1.29	0.67± 0.87	1.52± 1.19	1±0.85	1.17± 0.84	1.00± 0.64	1.06± 0.83	0.67± 0.49	0.73± 0.47	1.19± 0.60	0.86± 0.58	0.64± 0.63	0.87± 0.69	1.26± 0.68	0.93± 0.72

a and b: Mean ± Std

696
697 **Table 2.** The $DRE_{eBC, ATM}$ efficiencies of the eBC from fossil fuel combustion (eBC_{fossil}) and the eBC from biomass burning ($eBC_{biomass}$) under the four featured atmospheric motions

	$DRE_{eBC_{fossil}, ATM}$ efficiency[a] ($(W\ m^{-2})/(\mu g\ m^{-3})$)	$DRE_{eBC_{biomass}, ATM}$ efficiency[a] ($(W\ m^{-2})/(\mu g\ m^{-3})$)
LD	10.2 ± 4.2	10.3 ± 4.4
LSRW	10.6 ± 5.7	10.2 ± 5.8
LWRS	13.5 ± 6.7	14.7 ± 8.1
RD	15.6 ± 8.9	15.5 ± 8.4

698 a: Mean ± Std

699

700 **Figure captions:**

701 **Figure 1.** Four factors identified by source apportionment. Concentration (μg m^{-3}) of the chemical species and b_{abs} (λ) at six

702 wavelengths (λ = 370, 470, 520, 590, 660, or 880nm) (M m^{-1}) in each source are colored by grey. The blue square represents

703 the contribution of each chemical species in the four different factors.

704 **Figure 2.** (a) The diurnal variations of the eBC from fossil fuel combustion (eBC$_{fossil}$), (b) the eBC from biomass burning

705 (eBC$_{biomass}$), (c) the wind speed (m s^{-1}) and (d) the planetary boundary layer height (m).

706 **Figure 3.** (a) The 75th – 100th percentile mass concentrations of the eBC from fossil fuel combustion (eBC$_{fossil}$) and (b) the eBC

707 from biomass burning (eBC$_{biomass}$) under local dominance (LD), local strong and regional weak (LSRW), local weak regional

708 strong (LWRS) and regional dominance (RD). S_{bj} is actual wind run distance at 100m height, R_{bj} is the recirculation factor.
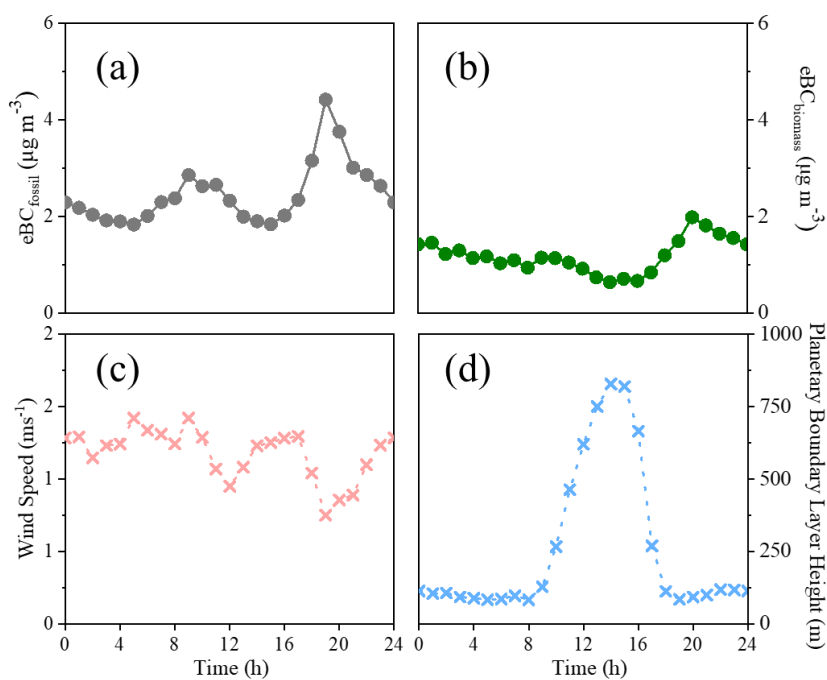
709 **Figure 4.** (a) The mass concentrations of the eBC from fossil fuel combustion (eBC$_{fossil}$) and (b) the eBC from biomass burning

710 (eBC$_{biomass}$) during daytime and (c,d) nighttime under local dominance (LD); local strong and regional weak (LSRW); local

711 weak regional strong (LWRS); and regional dominance (RD).

712 **Figure 5.** Direct radiative effect (DRE) of the eBC from fossil fuel combustion (eBC$_{fossil}$) and the eBC from biomass burning

713 (eBC$_{biomass}$) (a) in the top atmosphere (TOA), surface (SUF), and in-between the atmosphere (ATM) and (b) the DRE$_{eBC,ATM}$ of

714 two types of eBC under local dominance (LD), local strong and regional weak (LSRW), local weak regional strong (LWRS)

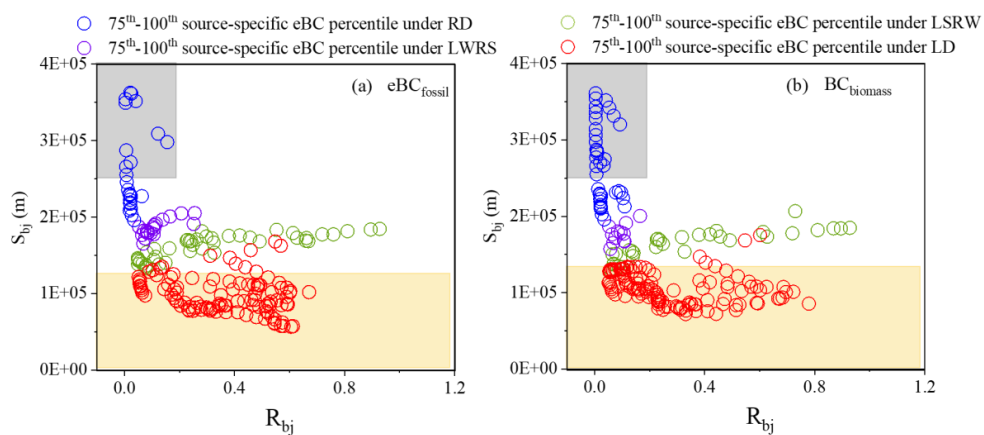715 and regional dominance (RD).

716
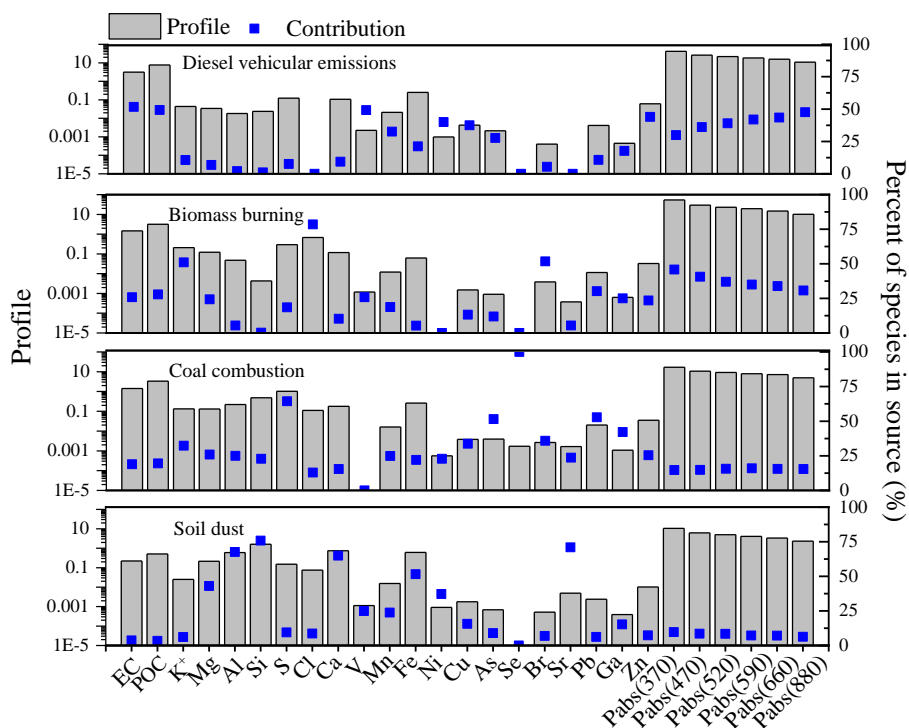
Figure 1. Four factors identified by source apportionment. Concentration ($\mu g\ m^{-3}$) of the chemical species and b_{abs} (λ) at six wavelengths (λ = 370, 470, 520, 590, 660, or 880nm) (M m^{-1}) in each source are colored by grey. The blue square represents the contribution of each chemical species in the four different factors.
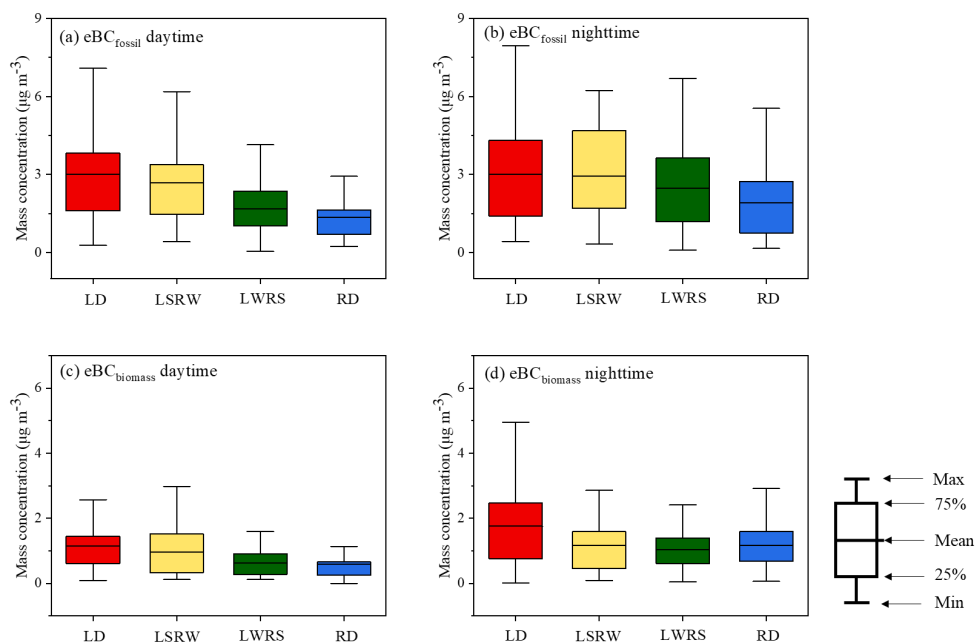
720

Figure 2. (a) The diurnal variations of the eBC from fossil fuel combustion (eBC$_{fossil}$), (b) the eBC from biomass burning
(eBC$_{biomass}$), (c) the wind speed (m s^{-1}) and (d) the planetary boundary layer height (m).

723

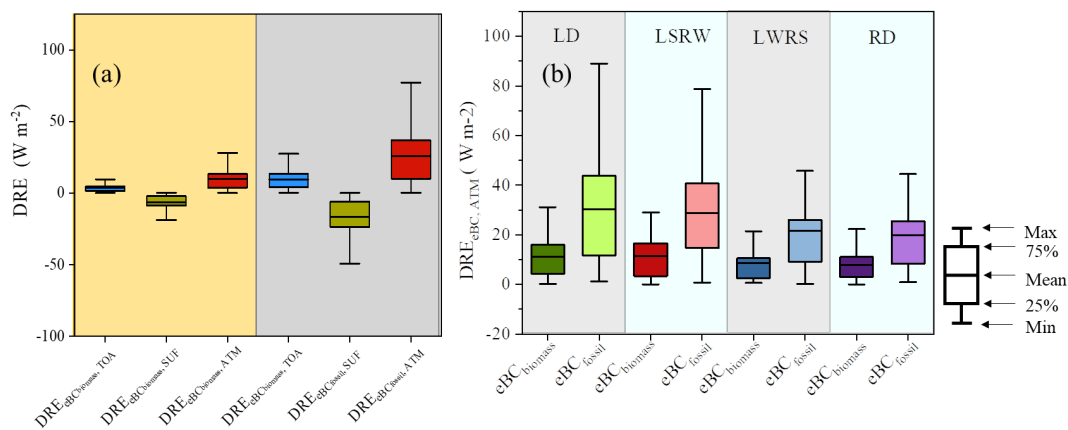**Figure 3.** (a) The $75^{th} - 100^{th}$ percentile mass concentrations of the eBC from fossil fuel combustion (eBC$_{fossil}$) and (b) the eBC

from biomass burning (eBC$_{biomass}$) under local dominance (LD), local strong and regional weak (LSRW), local weak regional

strong (LWRS) and regional dominance (RD). S_{bj} is actual wind run distance at 100m height, R_{bj} is the recirculation factor

Figure 4. (a) The mass concentrations of the eBC from fossil fuel combustion (eBC$_{fossil}$) and (b) the eBC from biomass burning (eBC$_{biomass}$) during daytime and (c,d) nighttime under local dominance (LD); local strong and regional weak (LSRW); local weak regional strong (LWRS); and regional dominance (RD).

Figure 5. Direct radiative effect (DRE) of the eBC from fossil fuel combustion (eBC$_{fossil}$) and the eBC from biomass burning (eBC$_{biomass}$) (a) in the top atmosphere (TOA), surface (SUF), and in-between the atmosphere (ATM) and (b) the DRE$_{eBC,ATM}$ of two types of eBC under local dominance (LD), local strong and regional weak (LSRW), local weak regional strong (LWRS) and regional dominance (RD).